Efficient hyper-reduced-order model (HROM) for thermal analysis in the moving frame

Yancheng Zhang, Alain Combescure, Anthony Gravouil

Efficient hyper-reduced-order model (HROM) for thermal analysis in the moving frame

Yancheng Zhang [1, 2] *, Alain Combescure [1, 2] and Anthony Gravouil [1, 2, 3]

LaMCoS, INSA-Lyon, Universit de Lyon, CNRS UMR 5259, 18-20 rue des Sciences, F69621 Villeurbanne, France
[2] *Chaire AREVA-SAFRAN, INSA de lyon, France*
[3] *Institut universitaire de France, France*

SUMMARY

The hyper-reduced-order model (HROM) is proposed for the thermal calculation with a constant moving thermal load. Firstly, the constant velocity transient process is simplified to a steady-state process in the moving frame. Secondly, the control volume is determined by the temperature rate, and the thermal equilibrium equation in the moving frame is derived by introducing an advective term containing the loading velocity. Thirdly, the HROM is performed on the control volume with a moving frame formulation. This HROM has been applied to the thermal loading on brick and ring disk specimens with a CPU gain of the order of 7 (10). In addition, two strategies are proposed for the HROM to improve its precision. Moreover, the high efficiency and high accuracy are kept for the parametric studies on thermal conductivity and amplitude of heat flux based on the developed HROM.

Received . . .

KEY WORDS: Finite element methods; hyper-reduced-order model; quasi-static thermal analysis; moving frame; control volume; streamline upwind PetrovGalerkin

1. INTRODUCTION

This paper presents a finite element(FE) formulation-based hyper-reduced-order model(HROM) for quasi-static thermal analysis. The formulation is suitable for modeling material processes such as welding and laser surfacing in a constant loading with a high efficiency.

Correspondence to: LaMCoS, INSA-Lyon, Universit de Lyon, CNRS UMR 5259, 18-20 rue des Sciences, F69621 Villeurbanne, France.

[†]Yancheng.Zhang@insa-lyon.fr (Y.Zhang), Alain.Combescure@insa-lyon.fr (A.Combescure), Anthony.Gravouil@insa-lyon.fr (A.Gravouil)

Quasi-static processes can be defined as processes, which are steady-state problems in either a stationary or a moving configuration, and the system variables may have history-dependent behavior [1]. A fixed (Lagrangian) frame (FF) formulation is usually adopted to model a history dependent quasi-static problem by a transient analysis. A typical example of a quasi-static process is welding process, where the transient thermal analysis in the FF is numerically solved using a time-increment approach with a number of increments varying from hundreds to thousands. Besides, the FF formulation also requires a fine mesh in the model or implementing an adaptive mesh in the critical region around the heat source [2][3][4]. As a result, it is inefficient to employ the FF formulation for quasi-static analyses from the computational point of view, especially for 3D optimisation with multiple analysis.

Recently, the moving frame (MF) formulation is adopted for the quasi-static process to reduce the computational cost [5]. This conception was originally proposed by Nguyen and Rahimian[6] for the plastic problem. By this transformation, the evolution of temperature field can be modelled as a steady-state problem in the MF: the enforcement of energy balance leads to a flow through a control volume, which yields the corresponding governing equation. As a result, the history of the temperature field in the MF can then be calculated along the path lines [7]. In the MF formulation, an advective term introduced in the equilibrium equation leads to spurious oscillations of the solution in a thin boundary layer near the outflow boundary. To control the advective-derivative term and stabilize the oscillations, an artifical term is added only along the streamline direction by Brooks and Hughes [8]. The technique used is the streamline upwind petrov-galerkin (SUPG) method. However, the solution of the steady-state problem with the MF formulation requires the appropriate specification of boundary conditions over inlet and outlet surfaces of the control volume. As proposed by Balagangadhar et al.[5], the surface flux boundary conditions at these surfaces are assumed to be consistent with the steady-state response of the studied field. However, the computation is still costly with moving frame (MF) formulation if the control volume is too large.

To reduce the computational complexity for optimization procedures or parametric analyses, the reduced-order model (ROM) can be a good choice [9]. The ROM is based on the projection of the full-order model onto low dimensional reduced bases. Usually, ROMs based on the proper orthogonal decomposition (POD) is proposed [10][11][12][13][14]. The primary step is to build the reduced-basis (RB) with the most dominant modes of the POD of the snapshots, which contain resolutions of problems involving large time spans or series of similar problems. Then the solution of this reduced problem is decomposed using POD and projects the full-order model onto low dimensional reduced bases [15]. In addition, various interpolation methods are reported to get the adaptive RB for parametric studies [16][12][17][18]. However, the accuracy of the ROM strongly depends on the relevancy of the selected RB [19][20][15]. Contrary to the POD-based ROM method, the Proper Generalized Decomposition (PGD)-based ROMs [21] have been more recently generalized to high-dimensional problems [22][23][24][25][26][27]. The aim of PGD is to approximate a space-time solution as a sum of products of space and time functions, and the PGD method is uaually coupled with the non-linear non-incremental LATIN solver [21] over the entire time interval.

In this work, the POD-based hyper-reduced-order model (HROM) is proposed for the quasi-static process, the model reduction is performed on the control volume with the MF formulation, while the reduced bases are obtained from a series of representive control volumes determined by

the temperature rate in the fixed frame. This HROM has been applied to the brick and ring disk specimens. Finally, parametric studies are performed on the thermal conductivity and the amplitude of heat flux.

2. UCED-ORDER MODEL BASED ON THE FIXED FRAME FORMULATION

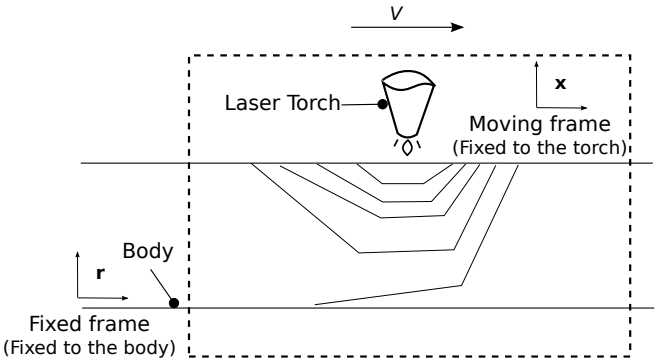

Figure 1. Fixed and moving frames

In the present work, a reference frame fixed to the material configuration, **r**, denotes a fixed frame (FF). In the FF, the torch moves with a constant velocity: the state of the body changes in time.

2.1. *Fixed frame formulation*

The equations in the FF are obtained by application of the energy balance equation. It yields the following governing equation for transient heat transfer analysis:

$$\rho C_p \frac{dT}{dt}(\mathbf{r},t) = \nabla \cdot (k\nabla T)(\mathbf{r},t) + Q(\mathbf{r},t) \tag{1}$$

where ρ is the density of the following body, C_p is the specific heat capacity, T is the temperature, k is the thermal conductivity, Q is the internal heat generation rate, t is the time, $\mathbf{r}$ is the coordinate in the reference configuration and $\bigtriangledown$ is the spatial gradient operator.

The initial temperature field is given by $T = T^0$ for the entire volume V, where T^0 is the prescribed initial temperature. The following boundary conditions are applied on the surfaces:

$$T^s = T^p \text{ on the surface } \Gamma_1, \text{ with prescribed temperature} \tag{2}$$

$$q^s = q^p \text{ on the surface } \Gamma_2, \text{ with prescribed heat flux} \tag{3}$$

where T and q represent the prescribed temperature and surface flux, respectively.

$$\nabla T \cdot \mathbf{n} = h(T^a - T) \text{ on the surface } \Gamma_3, \text{ for convective heat transfer} \tag{4}$$

where $\mathbf{n}$ is the unit outward normal to the surface Γ_3, T^a is the external ambient temperature.

After integration by parts and the divergence theorem on the integral form of Eq.1 with Eqs.3 and 4, the weak form can be expressed by:

$$\int_{\Omega}\left[\nabla\hat{T}\cdot k\nabla T+\hat{T}\rho C_p\frac{dT}{dt}-\hat{T}Q\right]d\Omega-\int_{\Gamma_2}\hat{T}q d\Gamma-\int_{\Gamma_3}\hat{T}h\left(T^a-T\right)d\Gamma=0 \tag{5}$$

2.2. *Finite element discretization in the fixed frame*

By applying FE discretization and numerical integration from Eq. 5, the global equilibrium equation can be expressed by

$$\mathbf{C}^{eq}\dot{\mathbf{T}}+\mathbf{K}^{eq}\mathbf{T}=\mathbf{P}^{eq} \tag{6}$$

where $\mathbf{C}$ is the matrix of specific heat capacity, $\mathbf{K}^{eq}$ is thermal conductance matrix, $\mathbf{P}^{eq}$ is the thermal loading vector and $\mathbf{T}$ is the nodal temperature vector. The matrices $\mathbf{K}^{eq}$ and $\mathbf{C}^{eq}$, and vector $\mathbf{P}$ are constructed by the elemental matrices as follows.

$$\begin{aligned}\mathbf{K}^{eq}&=\Sigma_e\mathbf{K}^e+\Sigma_e\mathbf{H}^e\\ \mathbf{C}^{eq}&=\Sigma_e\mathbf{C}^e\\ \mathbf{P}^{eq}&=\Sigma_e\mathbf{P}^e_Q+\Sigma_e\mathbf{P}^e_q+\Sigma_e\mathbf{P}^e_H\end{aligned} \tag{7}$$

The explicit form of the elemental matrices is given below:

$$\begin{aligned}\mathbf{K}^e&=\int_{\Omega^e}k\left(\mathbf{B}\right)^T\mathbf{B}d\Omega\\ \mathbf{H}^e&=\int_{\Gamma_3^e}h\mathbf{N}^T\mathbf{N}d\Gamma\\ \mathbf{C}^e&=\int_{\Omega^e}\rho C_p\mathbf{N}^T\mathbf{N}d\Omega\\ \mathbf{P}^e_Q&=\int_{\Omega^e}Q\mathbf{N}^T d\Omega\\ \mathbf{P}^e_q&=\int_{\Gamma_2^e}q\mathbf{N}^T d\Gamma\\ \mathbf{P}^e_H&=\int_{\Gamma_3^e}hT^a\mathbf{N}^T d\Gamma\end{aligned} \tag{8}$$

By the discretisation in time field, the above spatial discretization equation can be expressed by

$$\mathbf{C}\quad\triangle t+\mathbf{K}^{eq}\theta\right)\mathbf{T}_{n+1}+\left(-\mathbf{C}^{eq}/\triangle t+\mathbf{K}^{eq}\left(1-\theta\right)\right)\mathbf{T}_n=\left(1-\theta\right)\mathbf{P}^{eq}_n+\theta\mathbf{P}^{eq}_{n+1} \tag{9}$$

where θ is the interpolation coefficient and defined as: $0\leq\theta\leq 1$. In this work, a backward difference with $\theta=1$ is adopted.

2.2.1. Creation of the reduced-basis (RB) The reduced basis is calculated by a matrix containing all solutions for each time t and for each benchmark problem $1\ldots S$. This matrix is constructed as follows:

$$\mathbf{T}_{\text{ref}}=\left[\mathbf{T}_1\ldots\mathbf{T}_S\right]$$

By performing a singular value decomposition (SVD) of the constructed reference matrix $\mathbf{T}_{\text{ref}}$ (n $>$ m), we can obtain the POD bases of the temperature field, Φ.

$$\mathbf{T}_{\text{ref}} = \Phi\,\Sigma\,\Upsilon^T = \begin{bmatrix}\Phi_1 & \cdots & \Phi_n\end{bmatrix} \begin{bmatrix}\sigma_1 & 0 & \cdots & 0\\ 0 & \sigma_2 & & \vdots\\ \vdots & & \ddots & 0\\ 0 & \cdots & 0 & \sigma_m\\ 0 & \cdots & 0 & 0\\ \vdots & \cdots & \vdots & \vdots\\ 0 & \cdots & 0 & 0\end{bmatrix} \begin{bmatrix}\Upsilon_1^T\\ \vdots\\ \Upsilon_m^T\end{bmatrix} \tag{10}$$

$\Phi \in$ $^{\times n}$ is a unitary matrix containing space vectors, $\Upsilon \in \mathbb{R}^{m\times m}$ a unitary matrix ectors, and $\Sigma \in \mathbb{R}^{n\times m}$ contains diagonal and non-negative singular values σ_i in a decreasing order.

2.2.2. Truncated SVD The following decomposition Eq.11 is the truncated SVD of $\mathbf{T}$. Approximation of the problem solution is faster when truncated SVD is used.

$$\mathbf{T}_{\text{ref}} \simeq \Phi_1\,\sigma_1\,\Upsilon_1^T + \Phi_2\,\sigma_2\,\Upsilon_2^T + \cdots + \Phi_i\,\sigma_i\,\Upsilon_i^T + \cdots + \Phi_k\,\sigma_k\,\Upsilon_k^T \tag{11}$$

where the mode number k is determined by Eq. 12 from a sens of energy, the sum of selected singular values should contain 99 % energy compared to that of the total one.

$$\eta_T = \frac{\Sigma_{i=1}^{i=k}\sigma_i}{\Sigma_{i=1}^{i=m}\sigma_i} \tag{12}$$

To better explain the Hyper-reduced-order model(HROM), the POD reduced-order model is firstly presented in the following sub-section.

2.2.3. POD reduced-order model The POD reduced-order model is actually a model reduction technique, in which the complete solution is projected onto a small dimensional subspace Φ[18]. Based on conventional FE method, the discrete form of the equilibrium equation at time step t can be expressed by the selected first modes of containing the largest part of "energy" of all modes:

$$\begin{aligned}(\Phi)^T\,(\mathbf{C}^{eq}/\triangle t + \mathbf{K}^{eq}\theta)\,\Phi\widetilde{\mathbf{T}}_{n+1} =\\ (\Phi)^T\,\{\mathbf{P}_n^{eq}(1-\theta) + \theta\mathbf{P}_{n+1}^{eq} - (-\mathbf{C}^{eq}/\triangle t + \mathbf{K}^{eq}(1-\theta))\,\mathbf{T}_n\}\end{aligned} \tag{13}$$

The resolution of the this system reduced the unknowns from m (the degree of freedom of the system) to k (the selected model number of Φ). As a result, an approximation of the solution $\mathbf{T} = \Phi\widetilde{\mathbf{T}}_{n+1}$ can be obtained very fast.

2.2.4. Hyper-reduced-order model (HROM) formulation in the fixed frame For the POD method, the number of constitutive equations that need to be resolved to estimate the temperature field is not modified. Indeed, the main computational cost is determined by the number of constitutive equations, especially for the nonlinear problem. One way to reduce the number of constitutive equations is to create a reduced integration domain (RID), where the calculation of constitutive equations is only considered. Moreover, the orthogonal condition in Eq. 13 does not mean that all the residuals of the equilibrium equations must be equal to zero, thus it allows us to introduce the RID only on a part of the global domain by the selection matrix Π.

With the selected modes of the POD bases Φ, the formulation of the HROM can be expressed by

$$\begin{aligned}(\Pi\Phi)^T\,\Pi\,(\mathbf{C}^{eq}/\triangle t+\mathbf{K}^{eq}\theta)\,\Phi\widetilde{\mathbf{T}}_{n+1}=\\ \Pi\Phi)^T\,\Pi\{\mathbf{P}_n^{eq}(1-\theta)+\theta\mathbf{P}_{n+1}^{eq}-(-\mathbf{C}^{eq}/\triangle t+\mathbf{K}^{eq}(1-\theta))\,\mathbf{T}_n\}\end{aligned} \tag{14}$$

where Π is a rectangular boolean matrix, which allows to perform the selection of degrees of freedom needed for the HROM. Usually, the components of first largest vaules of the selected modes are considered, more details can be referred to Ryckelynck [11] and Zhang et al. [18]. Finally, the temperature field is obtained for the entire model by

$$\mathbf{T}_{n+1}=\Phi\widetilde{\mathbf{T}}_{n+1} \tag{15}$$

2.2.5. Difficulties of applying HROM in the fixed frame From the transient thermal analysis as sescribed in sub-section 4.1 for a moving thermal load on a brick specimen, the snapshots of all time steps are collected as the $\mathbf{T}_{\text{ref}}$. To obtain enough mode number for representing the reference matrix $\mathbf{T}$, the singular value decomposition(SVD) is performed on the temperature and temperature increment of the whole model. The obtained plots are given in Fig. 2.

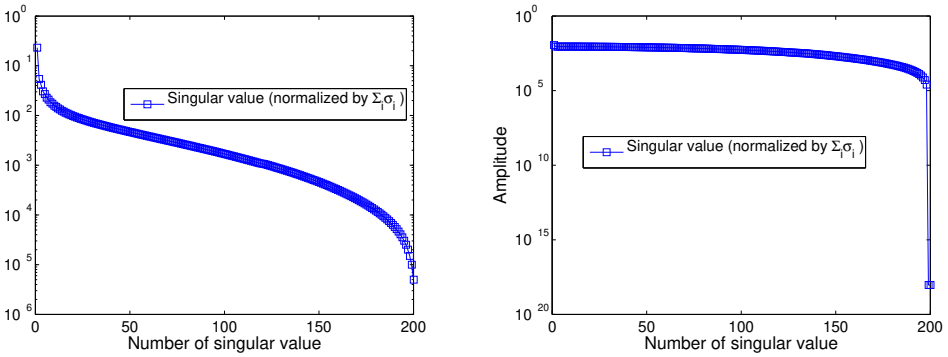

(a) SVD on temperature (b) SVD on temperature increment

Figure 2. SVD on temperature evaluation of the entire model of the brick specimen

By SVD on temperature Fig. 2(a), 147 modes are needed to get a ratio of 99% for the singular value from a sense of energy by Eq. 12, which leads to more selected elements in the RID. So it's not practical to adopt the POD bases of temperature field for the entire model. Then the SVD

on temperature increment is performed in Fig. 2(b). Unfortunately, almost all the singular values give the same amplitude, and 171 modes have to be considered for the POD bases of temperature increment. Obviously, the above two choices defeat the purpose of model reduction and limit the efficiency of the reduced POD models.

Fortunately, the SVD on temperature field in the control volume at the stabilized time steps can resolve the above mentioned problem, which will be introduced in the following section.

3. R-REDUCED-ORDER MODEL BASED ON THE MOVING FRAME FORMULATION

In this section, the quasi-static problem is considered as a steady-state problem in a moving frame (MF) formulation. Moreover, the hyper-reduced-order model is proposed based on the MF formulation in a control volume.

3.1. Moving frame formulation

Let us consider the case where the velocity and heat input are constant, the body is infinitely long in the direction of the velocity and its shape is uniform along that direction: the state of the body does not change in time if the moving frame (MF) **x** is fixed to the torch (Fig. 1).

In the MF system, a reference configuration is fixed both in space and time. The material configuration is moving at a velocity $-\mathbf{v}$ with respect to the reference configuration. As a result, the reference configuration is a control volume through which the material flows (Fig. 3). For a solid body flowing through a control volume, the equation with zero viscous dissipation is derived by enforcing energy balance over the control volume [1].

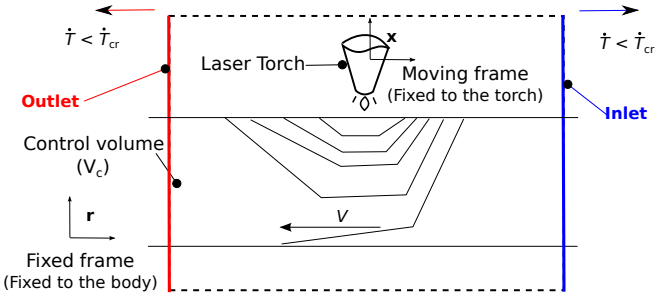

Figure 3. Moving frame in the control volume

$$\rho C_p \frac{dT}{dt} = \nabla \cdot (k \nabla T) + Q \tag{16}$$

The derivative of temperature in the flowing body with respect to time is given by

$$\frac{dT}{dt} = \frac{\partial T}{\partial t} + \frac{\partial T}{\partial x_i}\frac{dx_i}{dt} \tag{17}$$

where x is the material system coordinate, translating with a velocity $-\mathbf{v}$ in space by Eq. 18

$$\mathbf{x} = \mathbf{r} - \mathbf{v}t \tag{18}$$

Then Eq.17 can be expressed as

$$\frac{dT}{dt} = \frac{\partial T}{\partial t} - \mathbf{v} \cdot \nabla T \tag{19}$$

For a body flowing with a steady constant velocity, Eq.16 yields

$$\rho C_p \frac{dT}{dt} - \rho C_p (\mathbf{v} \cdot \nabla T) = \nabla \cdot (k \nabla T) + Q \tag{20}$$

Actually, Eq. 20 represents the transient MF equation. As we look for the stationary process which should have a constant heat input and flow velocity in the control volume. The control volume will then have a steady state temperature profile. Then the MF equation for a quasi-static process can be simplified as follows:

$$-\rho C_p (\mathbf{v} \cdot \nabla T) = \nabla \cdot (k \nabla T) + Q \tag{21}$$

The boundary conditions in the MF configuration are similar to those in the fixed configuration. The temperature and the heat flux boundary conditions are given by Eqs.2 and 3. However the boundary conditions are modelled separately, since time is mapped onto space in the MF configuration. The new boundary conditions are given by

$$T = T^0 \text{ on the surface, entering into the control volume} \tag{22}$$

$$T = T^{out} \text{ on the surface, going out of the control volume} \tag{23}$$

By the boundary condition of Eqs. 3 and 4, the weak form of Eq.16 can be expressed by

$$\int_\Omega \left[\nabla \hat{} \cdot k \nabla T - \hat{T} \rho C \mathbf{v} \cdot \nabla T - \hat{T} \rho Q\right] d\Omega - \int_{\Gamma_2} \hat{T} q d\Gamma - \int_{\Gamma_3} \hat{T} h (T_a - T) d\Gamma = 0 \tag{24}$$

For the weak form of MF formulation Eq.24, the boundary conditions Eq.2, Eq.22 and Eq. 23 are stongly enforced. However, the temperature (Eq.23) on the outlet surface is not yet known at this time.

3.2. *Finite element discretization*

By applying FE discretization and numerical integration from Eq. 24, the equilibrium equation is given by

$$(\mathbf{C}^{eq} + \mathbf{K}^{eq})\mathbf{T} = \mathbf{P}^{eq} \tag{25}$$

where $\mathbf{C}^{eq} = \Sigma_e \mathbf{C}^e$ is the matrix of specific heat capacity containing the material flowing velocity, and $\mathbf{C}^e$ is expressed by $\mathbf{C}^e = \int_{\Omega^e} \rho c \mathbf{N}^T \mathbf{v}^T \mathbf{B} d\Omega$.

3.3. Hyper-reduced-order model

Since the temperature field is assumed to be sufficiently uniform in the velocity direction near the inlet and outlet edges, an approximate zero surface flux is prescribed across the boundaries as proposed by Balagangadhar et al.[5].

Therefore in the MF, the problem becomes a stationary one, where the coordinate x is in a control volume through which the material configuration flows. The hyper-reduced-order model (HROM) is performed on the control volume, and the reduced bases can be obtained from SVD of temperature field from a series of control volumes. Specifically, the temperature field should be extracted by the frame transformation.

$$\mathbf{T}(\mathbf{x},t_i) = \mathbf{T}(\mathbf{r},t_i) \text{ with } \mathbf{x} = \mathbf{r} \text{ - } \mathbf{v}\,\mathrm{t} \tag{26}$$

3.3.1. Control volume determination The question is now following: how to determine the representative control volume for the SVD analysis? In this work, the temperature rate is evaluated to find both inlet and outlet surfaces. Let us define:

$$\dot{T} = \frac{\Delta T}{\Delta t} \tag{27}$$

t the control volume is determined by V_c = | volume in V_{global} such that $\dot{T} >= \dot{T}_{cr}$ as shown in Fig. 3. If the velocity of heat source is not known, the temperature rate can be also used to determine the velocity direction by post-processing of the temperature distribution.

3.3.2. Hyper-reduced-order model in the moving frame It should be mentioned that the SVD operation is performed on the control volumes. With the selected modes of the POD bases Φ, the formulation of the HROM can be expressed by

$$(\Pi\Phi)^T \Pi (\mathbf{K}_{eq} + \mathbf{C}_{eq}) \Phi\widetilde{\mathbf{T}} = (\Pi\Phi)^T \Pi \mathbf{P}_{eq} \tag{28}$$

Finally, the temperature field is obtained for the control volume by $\mathbf{T} = \Phi\widetilde{\mathbf{T}}$.

As the temperature rate is assumed to be uniform at both inlet and outlet of the control volume, the temperature of the whole domain can be resolved with few elements in the control volume.

3.3.3. Selection of reduced integration domain (RID) To select the elements in the reduced integration domain (RID) for the HROM, the gradient in the thermal loading direction V on the POD bases is evaluated by Eq.29. To avoid the ill-posed problem of Eq. 28, 10 maximum components of each gradient basis are selected to get enough elements for HROM analysis.

$$\Phi_{GV} = \mathbf{v}^T \frac{\partial \Phi}{\partial \mathbf{x}} = \mathbf{v}^T \mathbf{B} \Phi \tag{29}$$

Besides, the error measure is defined by Eq. 30

$$\varepsilon_T = \frac{\|\mathbf{T}_{HROM} - \mathbf{T}_{FE}\|}{\|\mathbf{T}_{FE}\|} \tag{30}$$

The CPU gain is defined as

$$T_{Gain} = \frac{t^{FE}}{t^{HROM}_{Online}} \tag{31}$$

4. APPLICATION OF HROM TO THE MOVING THERMAL LOADS

The objective of this section is to apply the HROM to the moving thermal loads on two typical workpieces: the brick and the ring disk with parallel inner and outer surfaces, where the same section areas (b h) and the section ratios of 4 (b/h or h/b) are adopted for the geometries of two workpieces (Figs. 4(b) and 14(b)).

4.1. Application to a brick specimen

As given in Fig. 4, the brick specimen is under a moving thermal load of V_y along the line of symmetry. Since the loading and the structure are symmetric, only half of the workpiece is considered and is discretized into 36000 TET4 elements and 10450 nodes. To simplify the thermal analysis, all the surfaces are assumed to be adiabatic except the loading point at the top surface.

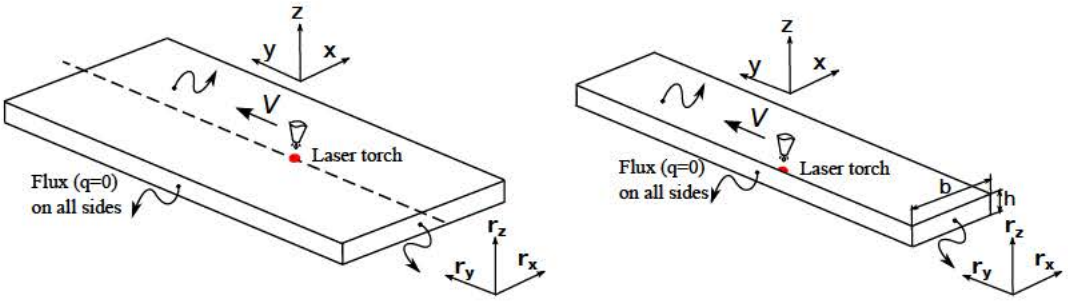

(a) Geometrical design (b) Problem adopted

Figure 4. Thermal loading set-up of the brick specimen

The detailed geometrical, loading and physical properties can be obtained from Tables. I and II. Besides, the laser diameter of 4 mm is adopted.

l (mm)	l (mm)	l_z(mm)	N.N	E.N	M.S.(mm)	E.T	H.F (W)	V_y(mm/s)
24	6	400	10450	36000	2.	TET4	480	4.

Notes: "N.N" means Node Number; "E.N" means Element number; "E.T" means Element type;"H.F" means Heat flux.; "M.S." means Mesh size

Table I. Geometrical description of the FE model of the brick specimen

The temperature evolution along line of symmetry obtained by the transient thermal calculation is given in Fig. 5(a). The temperature profiles present the similar tendency except the initial and final few time steps. The temperature profiles of time steps 99 and 180 are extracted in Fig. 5(b). The temperature profile of time step 99 is shifted onto to that of time step 180: the two profiles are the same except the boundary edge part for the temperature profile of time step 99.

Besides, the temperature profiles in the plane of symmetry are also presented in Fig. 6(a), where four parallel lines along the velocity direction are selected: L_1, L_2, L_3, L_4. It can be seen that

Notation	Name	Values
C_p	Specific heat capacity	710.0 J.kg^{-1}.K^{-1}
λ	Thermal conductivity	46.1 W.m^{-1}.K^{-1}
ρ	Density	7 850 kg.m^{-3}
T_0	Initial temperature	25. °C

Table II. Thermal parameters of the studied problem of the brick specimen

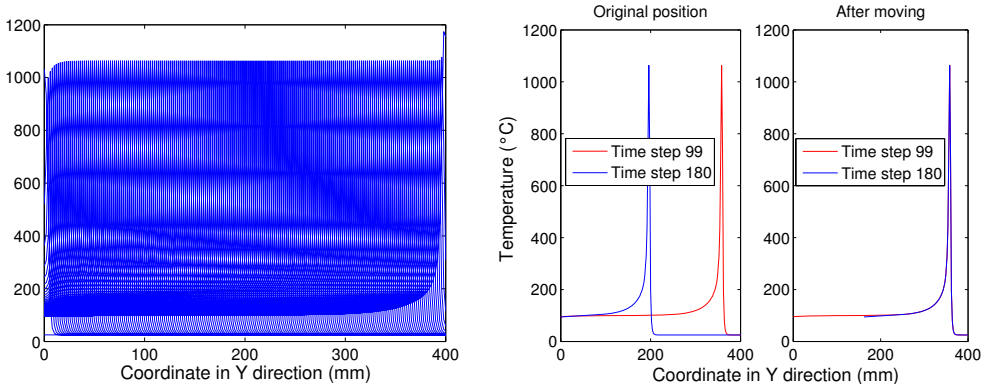

(a) Temperature along the line of symmetry (b) Selection analysis

Figure 5. Temperature evolution along the line of symmetry of the brick specimen

the temperature is already stabilized after 200 mm along the velocity direction V_y, and all the temperature values behind the loading points converge to around 100°C, which agrees with the assumption of Balagangadhar et al.[5].

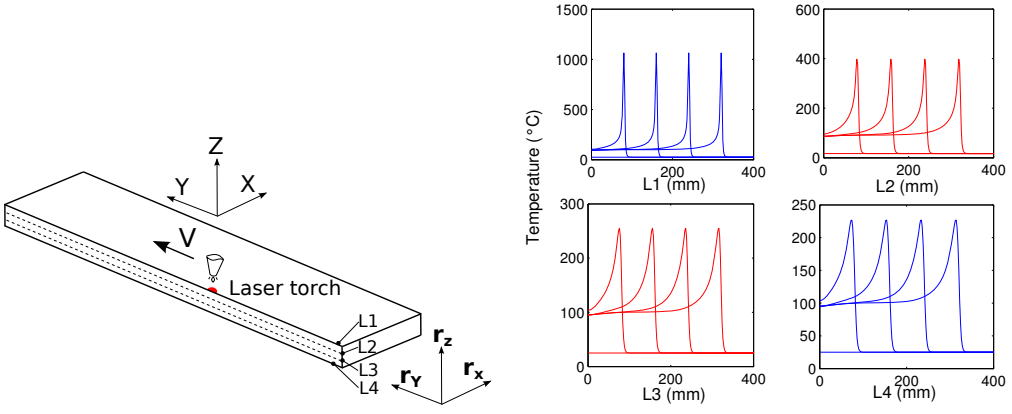

(a) Lines in the plane of symmetry (b) Temperature profiles of the lines

Figure 6. Temperature profile in the plane of symmetry of the brick specimen

4.1.1. Control volume determination for the brick specimen Following the assumption of the uniform temperature distribution near inlet and outlet, the control volume is determined by the temperature rate (Eq. 27) as shown in Fig. 7 with a critical value of $\dot{T} = 0.1$ °C/s.

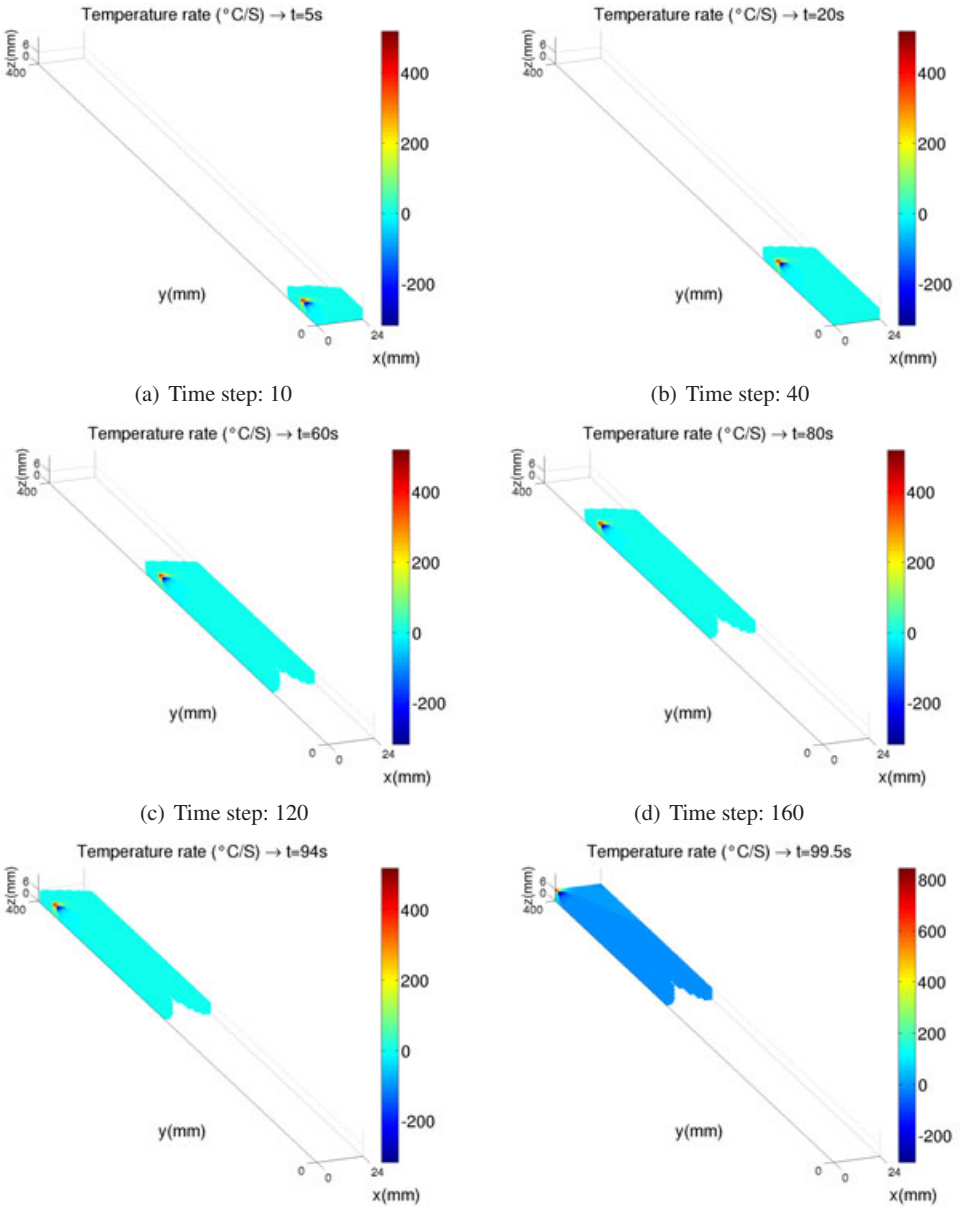

(a) Time step: 10 (b) Time step: 40

(c) Time step: 120 (d) Time step: 160

(e) Time step: 188 (f) Time step: 199

Figure 7. Temperature rate evolution with a critical value of 0.1 (°C/s) of the brick specimen

At the inital stages, the high ratio values located at the loading point near the boundary surface(Fig. 7(a)). After a few time steps, the rate profile stabilizes to a constant shape and size, as shown from time steps 40 to 188 (Figs. 7(b) to 7(e)), and this constant shape can be chosen as a control volume. Similarly to the initial stage, the different temperature ratio profile is also given in the final stage (Fig. 7(f)). To avoid the curved boundary surface, the sectional surfaces locate at y_{max} and y_{min} are considered as the inlet and outlet surfaces, respectively. As a result, the volume between inlet and outlet surfaces is chosen as the control volume.

Finally, the representative control volume (Fig. 8(a)) contains 16200 elements. It's interesting to plot the temperature distribution of the rest part of the workpiece in Fig. 8(b): the temperature of the part behind the control volume converges to 100 °C, which corresponds to Fig. 6(b); the part ahead of the control volume keeps its initial temperature. However, with the present control volume, the computation is still costly for linear thermal properties or future thermo-elasto-plastic problem. The hyper-reduced-order model(HROM) is then proposed for the control volume.

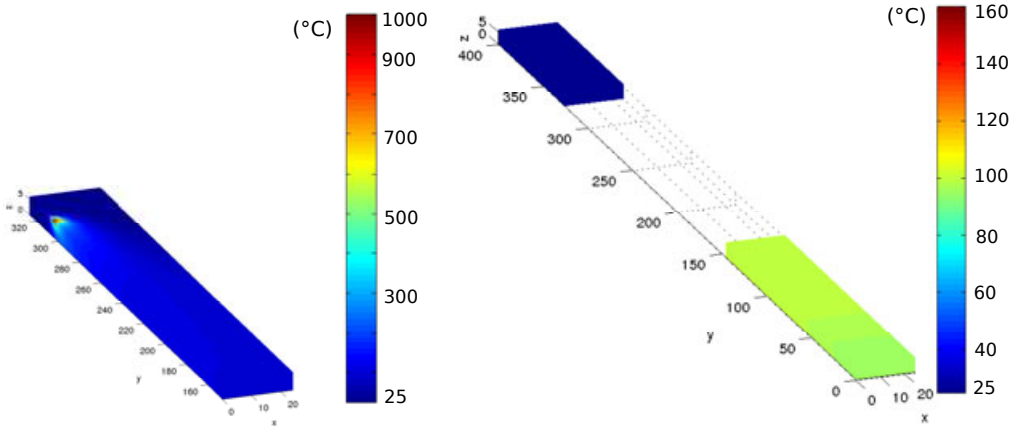

(a) The control volume (b) The rest part

Figure 8. Temperature distribution in the control volume at time step 152 of the brick specimen: 16200 elements, 4732 nodes

4.1.2. Model reduction for the brick specimen By the SVD of control volume of 46 stabilized time steps (from time steps 143 to 188), the plot of the normalized singular values is given in Fig. 9. Only one mode is needed to obtain 99% energy for the model reduction according to Eq. 12.

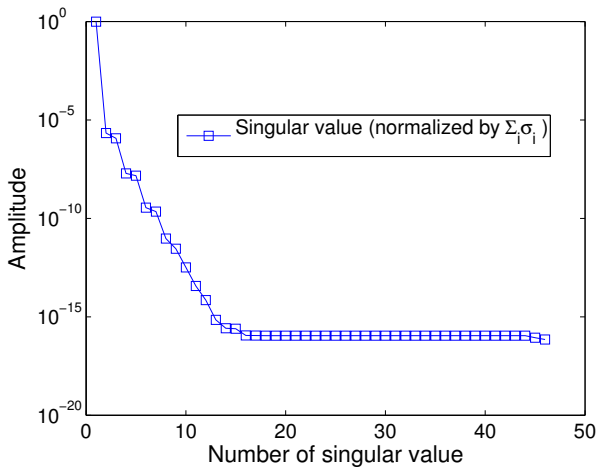

Figure 9. SVD on the temperature of the control volumes of the brick specimen

In the following part of this sub-section, parametric studies are performed on the precision of the temperature distribution by the different mode and temperature rate. It should be mentioned that

10 maximum values of the temperature gradient of each selected basis is adopted to obtain enough elements in the RID, more details can be referred to Ryckelynck [11] and Zhang et al. [18].

For the fixed temperature rate of $\dot{T}$ = 0.1 °C/s:

Cases	Selection ratio				C.V.(V_c)		RID. elements	
	Mod.	M.N.S.	τ(s)	$\dot{T}$(°C/s)	E.	N.	E.	N.
Case1	1	10	-	0.1	16200	4732	80	14
Case2	2	10	-	0.1	16200	4732	80	14
Case3	3	10	-	0.1	16200	4732	144	28
Case4	4	10	-	0.1	16200	4732	214	48
Case5	1	10	-	0.15	14940	4368	80	14
Case6	2	10	-	0.15	14940	4368	144	28
Case7	1	10	-	0.2	14220	4160	80	14
Case8	2	10	-	0.2	14220	4160	144	28
Case9	1	10	-	0.3	13140	3848	80	14
Case10	2	10	-	0.3	13140	3848	144	28
Full model	-	-	-	-	36000	10450	-	-

Notes: Mod.: Modes; M.N.S.: The number of the maximum values of each selected basis gradient; τ: Scaling Coefficient; C.V.: control volume; E.: Elements; N.: Nodes; RID.: Reduced integration domain

Table III. RID information of different mode and temperature rate of the brick specimen

Cases	C.T.(s)			Error(%)	
	Off.	On.	T_{Gain}	Glo.	M.T.
Case1	641.78	$2.28e^{-4}$	$1.02\ e^{8}$	11.82	11.82
Case2	633.32	$2.96e^{-4}$	$7.85\ e^{7}$	291.16	165.54
Case3	636.38	$1.41e^{-4}$	$1.65\ e^{8}$	2.30	0.27
Case4	637.89	$1.52e^{-4}$	$1.53\ e^{8}$	0.059	0.060
Case5	564.40	$3.15\ e^{-5}$	$6.62\ e^{8}$	11.82	11.82
Case6	563.68	$6.90\ e^{-5}$	$3.37\ e^{8}$	0.53	0.53
Case7	515.86	$3.00\ e^{-5}$	$7.74\ e^{8}$	11.82	11.82
Case8	518.76	$8.20\ e^{-5}$	$2.83\ e^{8}$	0.53	0.53
Case9	456.65	$2.40\ e^{-5}$	$9.68\ e^{8}$	11.82	11.82
Case10	463.52	$7.90\ e^{-5}$	$2.94\ e^{8}$	0.53	0.53
Full model	-	23229.96	-	-	-

Notes: C.T.: Computational time; Off.: Offline; On.: Online; Glo.: Global; M.T.: Maximum Temperature.

Table IV. Simulation results of different mode and temperature rate of the brick specimen

With one mode, 80 elements are selected in thermal loading zone of the control volume at time step 152, as shown in Figs. 10(a) and 10(b). The predicted temperature distribution of all the nodes and the nodes along Line1 in the control volume are given in Figs. 11(a) and 11(b), respectively.

By the temperature distribution along Line1 for 1 mode at $\dot{T}$ = 0.1 °C/s, the temperatures near the inlet well agree with the one from full model obtained by transient thermal calculation, while the values of the thermal loading point and near the outlet show difference compared to these of the full model, where the temperature in the loading point presents the same error (around 11.82%) as that of all the nodes in the control volume. Besides, the CPU gain of 10^8 is obtained. By 2 modes, the selected elements (case2 in Table III) are the same as the case of the 1 mode, which leads to high error (case2 in Table IV). It means the ill-posed reduced problem occurs (Zhang et al. [18] and Ryckelynck [11]). Then more elements (144) are selected with 3 modes near the inlet surface

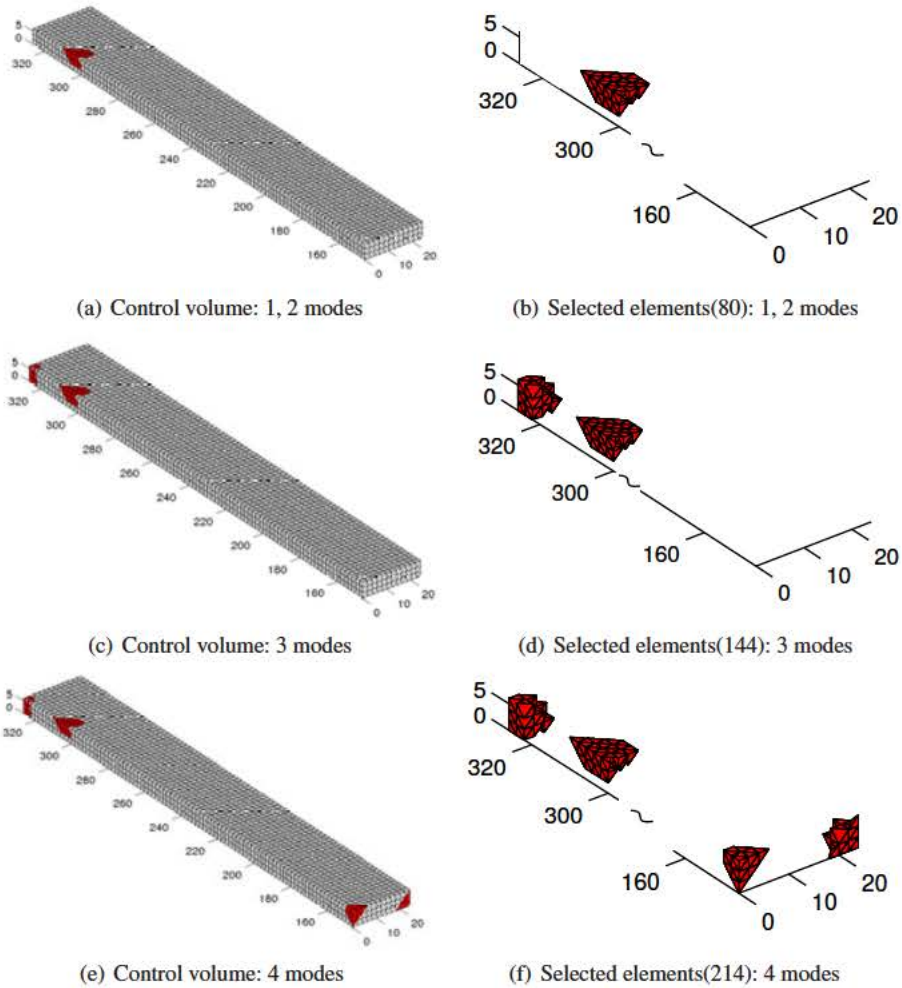

(a) Control volume: 1, 2 modes

(b) Selected elements(80): 1, 2 modes

(c) Control volume: 3 modes

(d) Selected elements(144): 3 modes

(e) Control volume: 4 modes

(f) Selected elements(214): 4 modes

Figure 10. Selected elements for HROM with different modes of the brick specimen

(Fig. 10(d)), which decreases the temperature error of the loading point to 0.27%. However, the disagreement near the oulet is still observed as shown in Fig. 11(d).

By increasing the mode number to 4, the selected elements extend from 144 to 214 with the additional elements at the outlet surface (Figs. 10(e), 10(f)), and the nodal temperatures on the inlet and outlet surface are strongly enforced. By the above consideration, the temperature error of all nodes decreases to 0.059 % by 4 modes finally (Fig. 11(e)), while the CPU gain keeps at 10^8.

Increasing the fixed temperature rate to $\dot{T}$ = 0.15 °C/s:

For $\dot{T}$ = 0.15 °C/s, less elements are selected for the control volume (14940 compared to 16200). With 1 mode, the same errors are obtained as the temperature rate of 0.1 °C/s, while acceptable errors are obtained with 2 modes for the enough selected elements in RID (case 6 in Table IV). Similar tendency is also found for the temperature rates of 0.2 °C/s (cases 7 and 8) and 0.3 °C/s (cases 9 and 10).

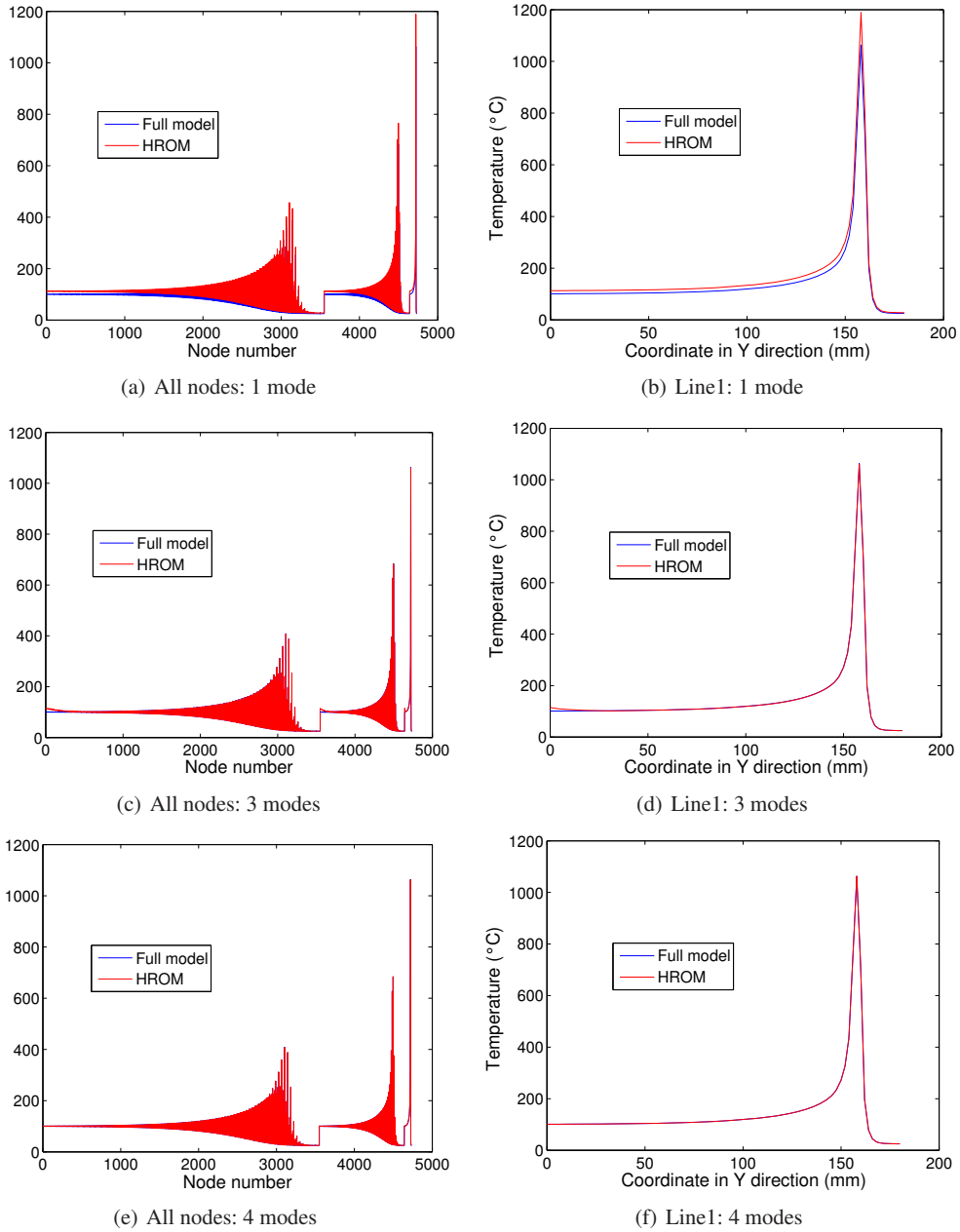

(a) All nodes: 1 mode (b) Line1: 1 mode

(c) All nodes: 3 modes (d) Line1: 3 modes

(e) All nodes: 4 modes (f) Line1: 4 modes

Figure 11. Temperature distribution in the control volume based on the HROM of the brick specimen

It should be mentioned that the error of 11.82% is obtained with mesh size of 2 mm and 1 mode, the error can continue to decrease with finer mesh (1 mm) and one mode, while the high computational cost is needed.

4.1.3. Stabilized streamline upwind PetrovGalerkin (SUPG) method To avoid mesh refining and the selection of elements at the boundary surfaces, the streamline upwind PetrovGalerkin (SUPG)

is adopted as prescribed in the work of Rajadhyaksha and Michaleris[1], then the weight function of the advective term is modified by adding $\tau \mathbf{v} \cdot \nabla T$

$$\int_{\Omega} \left[\nabla \hat{} \cdot \nabla \right] - \left(\hat{T} + \tau \mathbf{v} \cdot \nabla T \right) \rho C \mathbf{v} \cdot \nabla T - \hat{T} Q \big] \, d\Omega - \int_{\Gamma_2} \hat{T} q d\Gamma - \int_{\Gamma_3} \hat{T} h \left(T_a - T \right) d\Gamma = 0 \quad (32)$$

where τ is a coefficient which has the dimension of time (s). The following discretization process and model reduction are similar to Eq.s 25 and 28.

By selecting appropriate scaling factor τ (from case1 to case4 in Table V), the good agreement (error of 1.40%) can be obtained by τ= -0.25(s) (Fig. 12, the CPU gain is of the order of 7 (10^7). The temperature profiles of all nodes and L_1 in the control volume are also given in Fig. 13.

With the scaling factor τ, the boundary conditions on the inlet and outlet surfaces is not necessary, while the value of τ needs to be determined is sensitive to different mesh size and loading velocity.

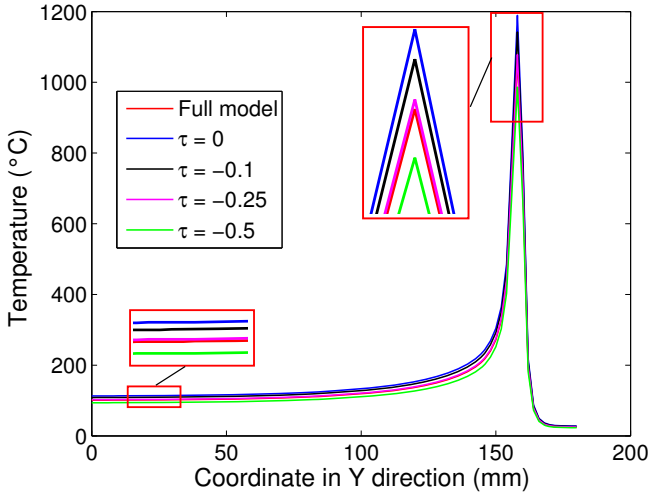

Figure 12. Temperature distribution on the L_1 based on the HROM with one mode and different scaling factors τ of the brick specimen

For the increased temperature rates (0.15, 0.2 and 0.3 °C/s), the same errors are obtained with less elements in control volumes (14940, 14220 and 13140 compared to 16200 for temperate rate 0.1°C/s), and the CPU gain keeps at 10^8, which means that the SUPG-based HROM can efficiently predict the temperature distribution with 1 mode and less elements in the control volume.

4.2. Application to ring disk

To present a general example of thermal loading, the ring disk structure is also adopted. Due to the symmetric loading and structure (Fig. 14(a)), only half of the structure is analyzed. The thermal loading is applied along the circular top edge line of the external radial surface (Fig. 14(b)) with a constant velocity of 4 mm/s and laser diameter of 4 mm. More detailed parameters are given in Table VII, where the internal and external radii are 74 and 80 mm, respectively. For the FE discretization, the mesh size of the radial external surface is also designed as 2 mm to keep consistent with that of the brick specimen.

Cases	Selection ratio				C.V.(V_c)		RID. elements	
	Mod.	M.N.S.	τ(s)	T(°C/s)	E.	N.	E.	N.
Case1	1	10	0.	0.1	16200	4732	80	14
Case2	1	10	-0.1	0.1	16200	4732	80	14
Case3	1	10	-0.25	0.1	16200	4732	80	14
Case4	1	10	-0.5	0.1	16200	4732	80	14
Case5	1	10	-0.25	0.15	14940	4368	80	14
Case6	1	10	-0.25	0.2	14220	4160	80	14
Case7	1	10	-0.25	0.3	13140	3848	80	14
Full model	-	-	-	-	36000	10450	-	-

Notes: Mod.: Modes; M.N.S.: The number of the maximum values of each selected basis gradient; τ: Scaling Coefficient; C.V.: Control volume; E.: Elements; N.: Nodes; RID.: Reduced integration domain

Table V. RID information of different scaling factor and temperature rate of the brick specimen

Cases	C.T. (s)			Error(%)	
	Off.	On.	T_{Gain}	Glo.	M.T.
Case1	641.78	$2.28e^{-4}$	$1.02\ e^{8}$	11.82	11.82
Case2	637.94	$2.40\ e^{-4}$	$9.68\ e^{7}$	7.40	7.40
Case3	636.29	$3.20\ e^{-4}$	$7.26\ e^{7}$	1.40	1.40
Case4	636.76	$2.31\ e^{-4}$	$1.01e^{8}$	7.25	7.25
Case5	564.28	$3.10\ e^{-5}$	$7.49e^{8}$	1.40	1.40
Case6	517.35	$3.10e^{-5}$	$7.49\ e^{8}$	1.40	1.40
Case7	456.08	$2.40e^{-5}$	$9.68\ e^{8}$	1.40	1.40
Full model	-	23229.96	-	-	-

Notes: C.T.: Computational time; Off.: Offline; On.: Online; Glo.: Global; M.T.: Maximum Temperature.

Table VI. Simulation results of scaling factor and temperature rate of the brick specimen

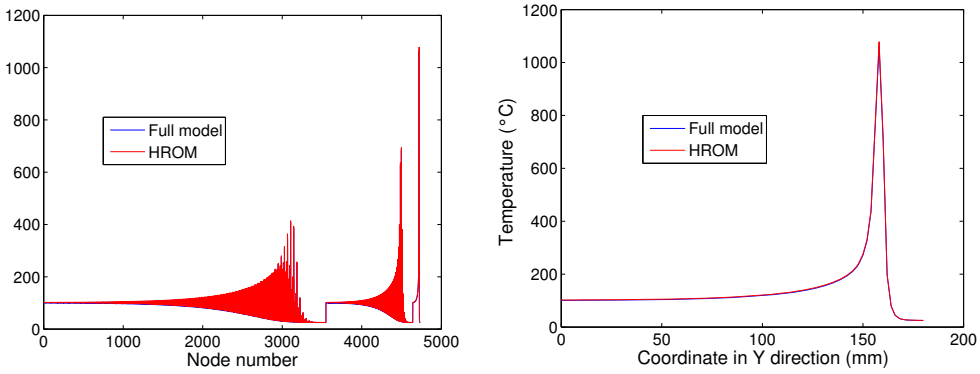

(a) All nodes: 1 mode, τ = -0.25 (s) (b) Line1: 1 mode, τ = -0.25 (s)

Figure 13. Temperature distribution in the control volume based on the SUPG and HROM of the brick specimen

R (mm)	$R_{Ou.}$(mm)	h(mm)	M.S.(mm)	N.N	E.N	E.T	H.F (W)	V (mm/s)
74	80	24	2	13052	54216	TET4	480	4

Notes: "In." means Inner; "Ou." means Outer; "M.S." means mesh size; "N.N" means Node Number; "E.N" means Element number; "E.T" means Element type;"H.F" means Heat flux.

Table VII. Geometry description of the FE model of the ring disk

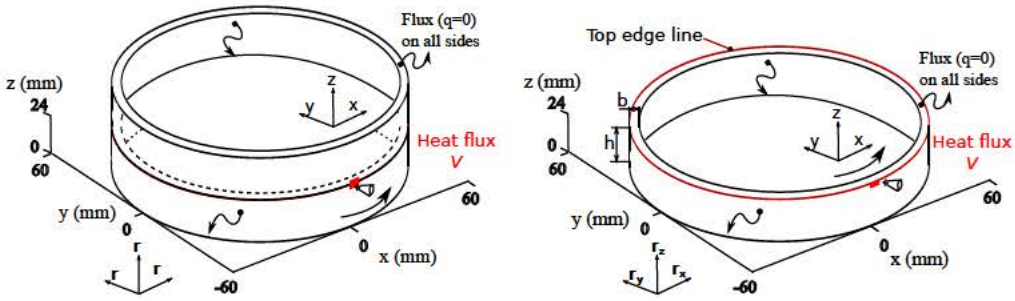

Figure 14. Geometrical model and boundary conditions of the ring disk

4.2.1. Control volume determination for the ring disk Firstly, the representative control volume must be determined by the critical temperature rate. By Eq. 27, the temperature rate larger than 0.15 C/s are given in Fig. 15. Similarly to the brick specimen, the geometry shape of temperature rate is not stable at the initial stage (Fig. 15(a), at time step 12). The regular profile starts to be stable after time step 136 (Fig. 15(c)), even in the final stage.

To avoid the curved boundary surface, the sectional surfaces locate at θ_{max} and θ_{min} are considered as the inlet and outlet surface, respectively. As a result, the volume between inlet and outlet surfaces is chosen as the control volume. The temperature distributions in control volume and the rest part are also given in Fig. 16 at time step 173 (86.5 s).

4.2.2. Model reduction for the ring disk Based on the control volume, 46 temperature field snapshots are selected from time steps 143 to 188. In the following step, the SVD is performed for the selected temperature snapshots, the singular values on temperature are distributed as shown in Fig. 17. Again, one mode contains 99 % energy.

To keep computational efficiency, only one mode is selected for present problem. In this case, 80 elements and 14 nodes are selected in the thermal loading zone (Fig. 18(b)). However, the errors for all nodes and the maximum temperature are larger than 10%. The the CPU gain is of the order of 7 (10). By keeping the FE equilibrium equation (Eq. 25), more modes are needed. When the mode number of 2 is selected, additional 45 elements are selected at the inlet (Fig. 18(d)), where the temperature of the additionally selected nodes are considered as the initial one (25 °C). Based on above HROM model in the control volume, the error of 0.60 % is obtained for all nodes and the maximum temperature, respectively. The temperature profile of the HROM also shows good agreements compared to that of FE model (Figs. 19(c), 19(d)), and the acceptable errors within 10% are obtained. The CPU gain still keeps at 10^7.

If we want to keep the computational efficiency, the SUPG strategy can be adopted with the scaling factor as mentioned in Eq. 32. Fortunately, the scaling coefficient τ with the same value of -0.25s also works for the circle thermal loading case. As given in Fig. 19(e), good agreement is obtained for all the nodes in the control volume. According the temperature plot along the loading edge (Fig. 19(f)), the stable temperature distributions ahead and behind the loading point can be easily observed, which proves the assumption for this more general loading case. Finally,

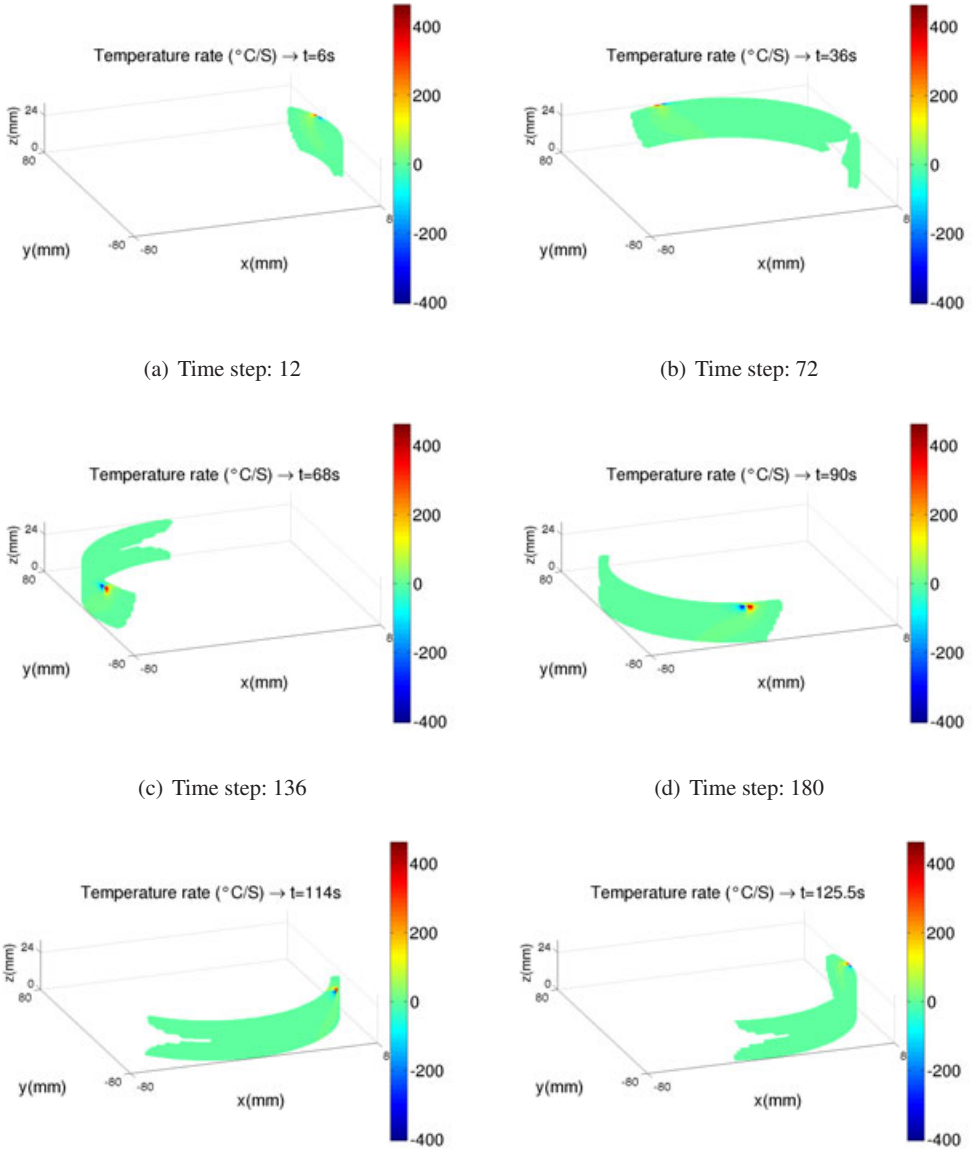

(a) Time step: 12 (b) Time step: 72

(c) Time step: 136 (d) Time step: 180

(e) Time step: 228 (f) Time step: 251

Figure 15. Temperature rate evolution larger than 0.15 (°C/s) of the ring disk

high precision with the controlled errors of 0.12% is obtained for all the nodes and top edge line, respectively. Further more, the CPU gain of 10^7 is still obtained.

It should be mentioned the SUPG strategy can be also ignored with further finer mesh (e.g.: 1 mm), which is similar to the case of the brick specimen.

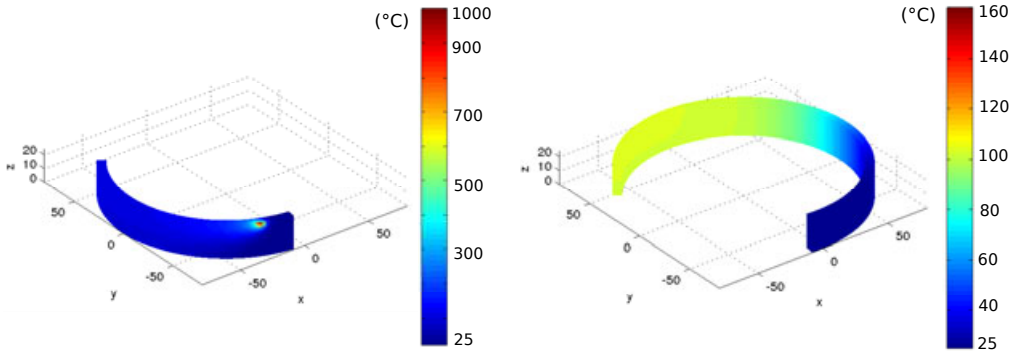

(a) Control volume (b) The reft part

Figure 16. Temperature distribution in the control volume at time step 173 (86.5 s) of the ring disk, elements: 18360, nodes: 4472

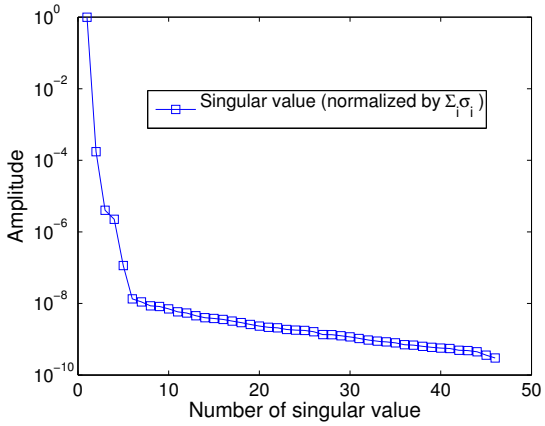

Figure 17. SVD on temperature snapshots of the ring disk

Cases	Selection ratio				C.V.(V_c)		RID. elements	
	Mod.	M.N.S.	τ(s)	T(°C/s)	E.	N.	E.	N.
Case1	1	10	-	0.15	18360	4472	80	14
Case2	2	10	-	0.15	18360	4472	125	24
Case3	1	10	-0.25	0.15	18360	4472	80	14
Full model	-	-	-	-	54216	13052	-	-

Notes: Mod.: Modes; M.N.S.: The number of the maximum values of each selected basis gradient; τ: Scaling Coefficient; C.V.: control volume; E.: Elements; N.: Nodes; RID.: Reduced integration domain

Table VIII. RID information of different cases of the ring disk specimen

Cases	C.T.(s)			Error (%)	
	Off.	On.	T_{Gain}	Glo.	M.T.
Case1	822.08	2.40e^{-4}	2.85 e^{7}	10.61	10.61
Case2	818.12	3.06 e^{-4}	2.22 e^{7}	0.16	0.16
Case3	822.27	2.22 e^{-4}	3.07 e^{7}	0.12	0.12
Full model	-	6804.74	-	-	-

Notes: C.T.: Computational time; Off.: Offline; On.: Online; Glo.: Global; M.T.: Maximum Temperature.

Table IX. Simulation resutls for different cases of the ring disk specimen

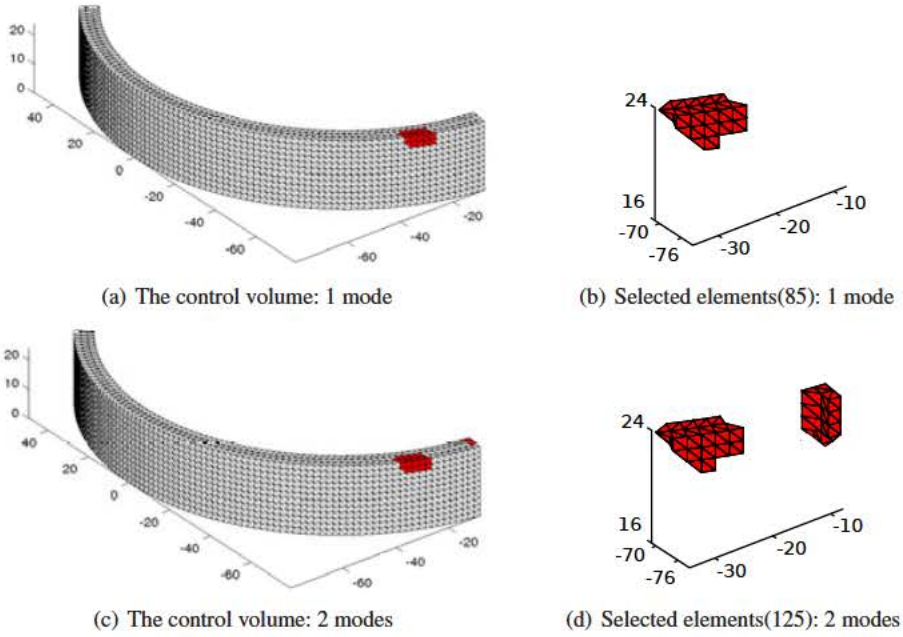

(a) The control volume: 1 mode (b) Selected elements(85): 1 mode

(c) The control volume: 2 modes (d) Selected elements(125): 2 modes

Figure 18. Selected elements in the control volume at time step 173 (86.5 s) of the ring disk

5. PARAMETRIC STUDIES

To check the versatility of the HROM, parametric studies are performed on thermal conductivity and the loading amplitude for the brick specimen, in which the Case2 is considered as the reference one for varying thermal and loading parameters. To keep the consistency for all cases, the temperature rate 0.1 °C/s is adopted to determine the control volume. By the constant loading amplitude, three different thermal conductivities of 36.1, 46.1 and 56.1 $W.m^{-1}.K^{-1}$ are employed, correponding to cases 1, 2 and 3 in Table X. With the temperature rate 0.1 °C/s, the element numbers of 18720, 16200 and 14580 are obtained for the control volume for cases 1, 2 and 3. It should be mentioned that the thermal conductivity is a very sentitive physical parameter for determining one stable thermal system according to simulation tests. For the lower thermal conductivity, more elements should be selected for the limited computational time and the stricted selection temperature rate 0.1 °C/s(less element number can be achived with higher selection temperature rate). For the higher thermal conductivity, the stable system is easily formed, then less elements are selected for the control volume. Actually, more strict selection temperature rate (small value) can be applied for higher thermal conductivity.

With the model number and the number of the maximum values of each selected basis gradient less than 10, the selected elements in the control volume are in the level of less than 400, where Case3 shows the highest value because of high mode number of 7. The Online computational times show that the HROM is quite efficiency for all the three cases, while the Offline computational time is greatly influenced by the number of control volume as given in Table XI. In addition, good agreements (Fig. 20) are obtained as well as the high CPU gain of 10^8.

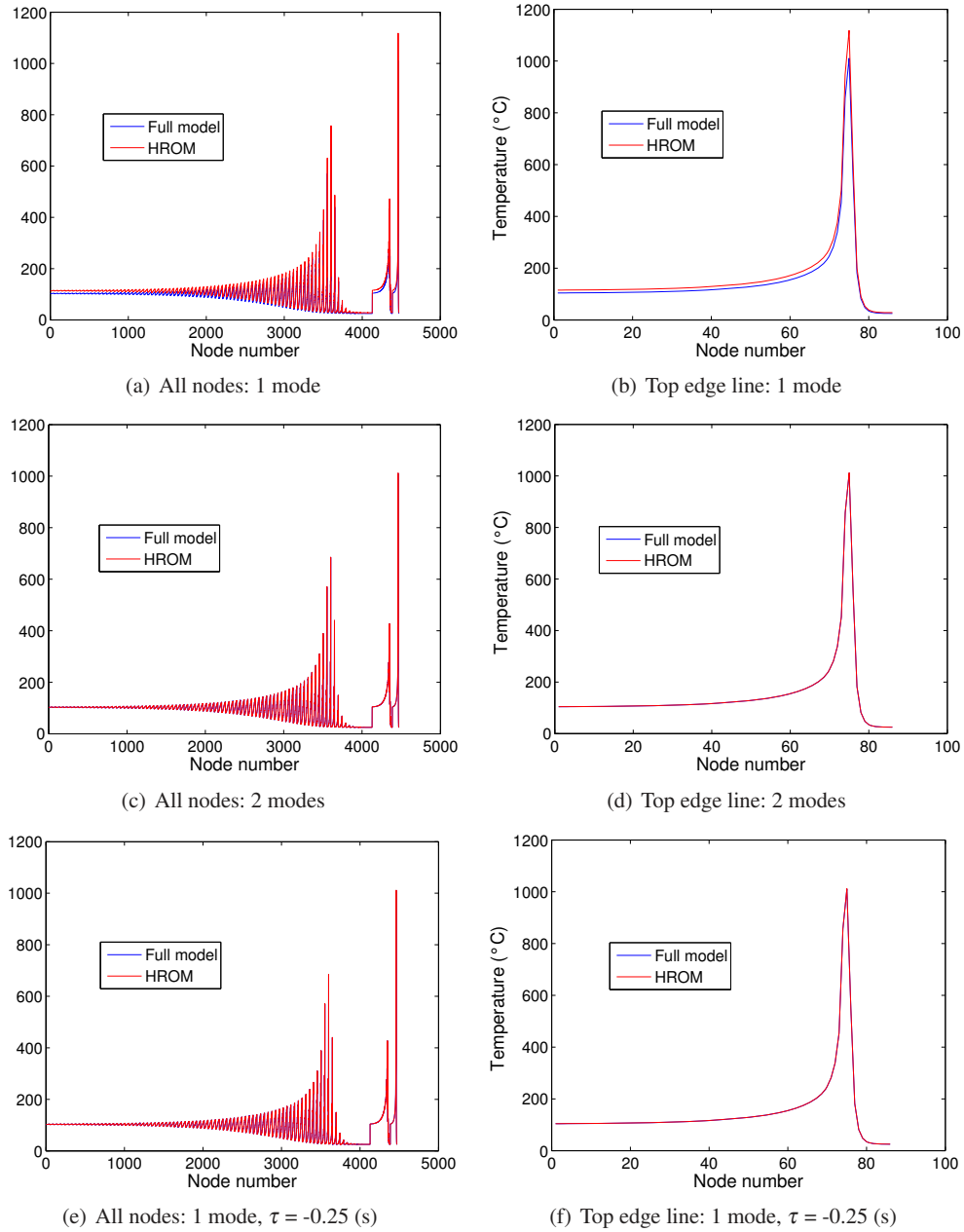

(a) All nodes: 1 mode (b) Top edge line: 1 mode

(c) All nodes: 2 modes (d) Top edge line: 2 modes

(e) All nodes: 1 mode, τ = -0.25 (s) (f) Top edge line: 1 mode, τ = -0.25 (s)

Figure 19. Temperature distribution in the control volume based on the HROM of the ring disk

Different values of heat flux of 440, 480 and 520 W for studying the effect of loading amplitude, corresponding to Cases 4, 2 and 5, are selected. As given in Table XI, the element number of the control volume increases with the laser power, while the variation of the elements in the control volume is less than 1000. Moreover, the selected elements and nodes for the RID show slight difference, similarly for the selected positions as shown in Figure 21. Due to few selected elements in the RID, the HROM always keeps high efficiency for all cases, and the good precision is kept with four modes as shown in Figure 21 and Table XI.

Cases	Conductivity	H.F.	Selection ratio			C.V.(V_c)		RID. elements	
			Modes	M.N.S.	T(°C/s)	E.	N.	E.	N.
Case1	36.1	480	4	10	0.1	18720	5460	214	48
Case2	46.1	480	4	10	0.1	16200	4732	214	48
Case3	56.1	480	7	10	0.1	14580	4264	357	75
Case4	46.1	440	4	10	0.1	16020	4680	229	48
Case5	46.1	520	4	10	0.1	16560	4836	214	48
Full model	-	-	-	-	-	36000	10450	-	-

Notes: H.F.: Heat flux; M.N.S.: The number of the maximum values of each selected basis gradient; τ: Scaling Coefficient; C.V.: control volume; E.: Elements; N.: Nodes; RID.: Reduced integration domain

Table X. RID information of different thermal conductivity with the same modes and temperature rate of the brick specimen

Cases	C.T.(s)			Error (%)	
	Off.	On.	T_{Gain}	Glo.	M.T.
Case1	712.89	1.72 e^{-4}	1.35 e^{8}	0.18	0.16
Case2	637.89	1.52 e^{-4}	1.53 e^{8}	0.059	0.060
Case3	572.59	1.63 e^{-4}	1.43 e^{8}	0.23	0.25
Case4	577.56	1.65 e^{-4}	1.41 e^{8}	0.089	0.092
Case5	654.71	1.76 e^{-4}	1.32 e^{8}	0.092	0.091
Full model	-	23229.96	-	-	-

Notes: C.T.: Computational time; Off.: Offline; On.: Online; Glo.: Global; M.T.: Maximum Temperature.

Table XI. Simulation results for parametric studies based on HROM for brick specimen

6. CONCLUSIONS

To resolve a quasi-static thermal process, an efficient hyper-reduced-order model(HROM) approach using one moving frame (MF) formulation has been proposed. The proposed model is achieved by the reduction of two times: 1) The control volume is selected to represent the whole model; 2) The HROM is applied to steady-state-based control volume.

The developed approach is applied to the moving thermal loading problems for brick and ring disk specimens. To increase the computational precision, two strategies are proposed: one can increase the mode number, which leads to more selected elements and decreases the computational efficiency (CPU gain of 10); one can also employ the streamline upwind PetrovGalerkin (SUPG) method, which keeps the highly computational efficiency with only one mode for a constant velocity (CPU gain of 10). However, the time dimensional scaling facor is necessary to be determined for different cases.

With the same cross section and mesh size for both brick and ring disk specimens under the same magnitude of thermal loading velocity, the scaling factor is independent of velocity direction. Based on the above two strategies, besides the high precision, the online run-times ratio of the HROM in the moving frame than the standard FE model in fixed frame is obtained at least by 7 orders of magnitudes (10).

Based on the proposed HROM, parametric studies on thermal conductivity and heat flux show high accuracy and high efficiency. The thermal conductivity is very sensitive for determining the control volume for maintaining the stable state, while the heat flux shows slight influence on the selected elements in the reduced integration domain.

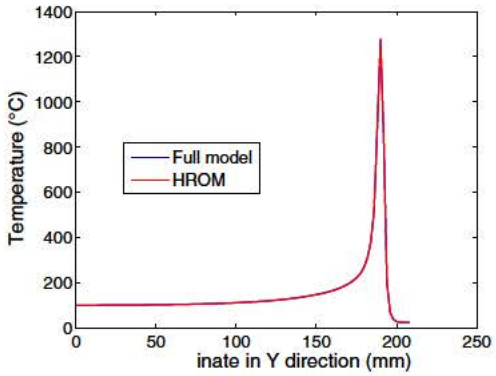

(a) Thermal conductivity 36.1: Temperature in L1

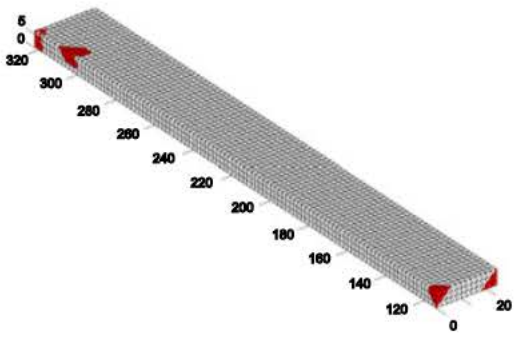

(b) Thermal conductivity 36.1: RID elements

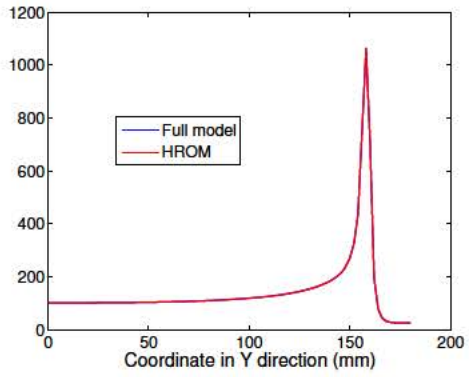

(c) Thermal conductivity 46.1: Temperature line

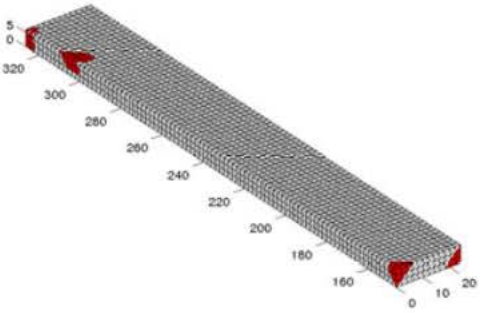

(d) Thermal conductivity 46.1: RID elements

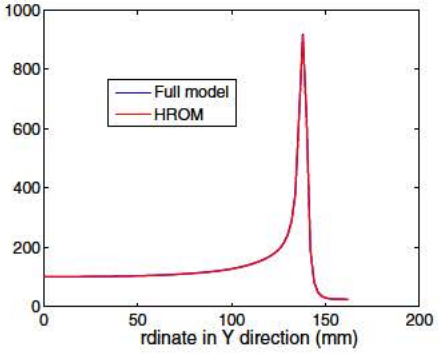

(e) Thermal conductivity 56.1: Temperature in L1

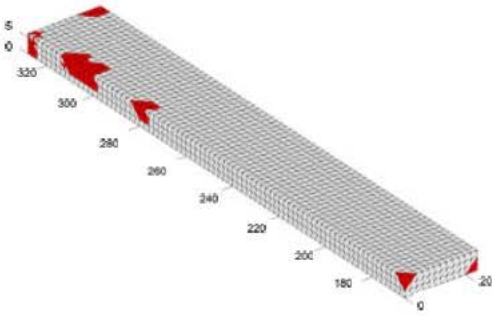

(f) Thermal conductivity 56.1: RID elements

Figure 20. Parametric studies on the thermal conductivity for the control volume based on the HROM of the brick disk

7. ACKNOWLEDGEMENTS

ACKNOWLEDGEMENT

The authors would like to acknowledge the AREVA-SAFRAN chair for the financial support.

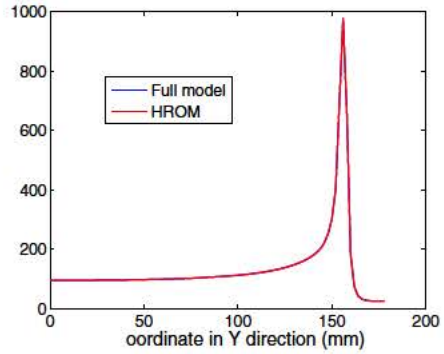

(a) Flux powder 440 W: Temperature in L1

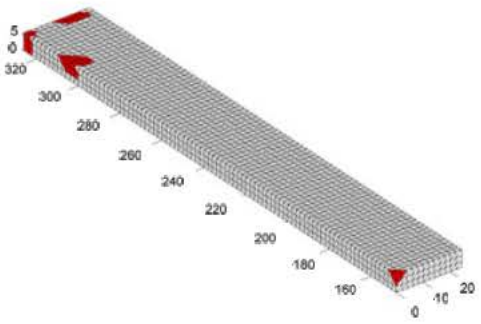

(b) Flux powder 440 W: RID elements

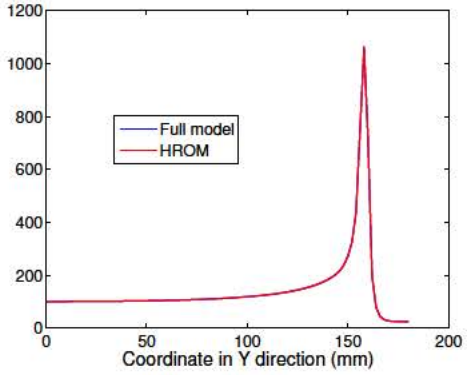

(c) Flux power 480 W: Temperature in L1

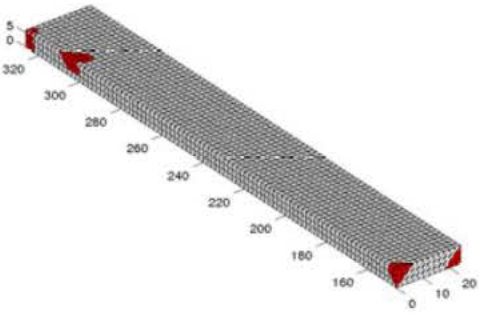

(d) Flux power 480 W: RID elements

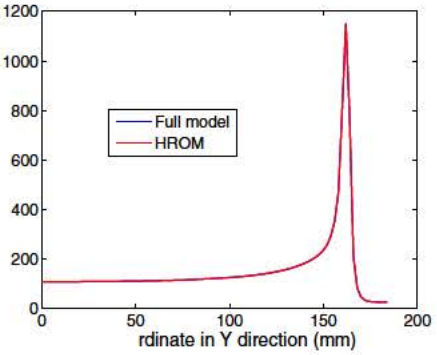

(e) Flux power 520 W: Temperature in L1

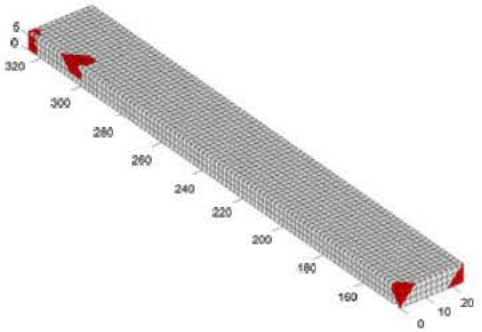

(f) Flux power 520 W: RID elements

Figure 21. Parametric studies on the loading amplitude for the control volume based on the HROM of the brick disk

REFERENCES

1. Rajadhyaksha S, Michaleris P. Optimisation of thermal processes using an eulerian formulation and application in laser surface hardening. *Internal journal for numerical methods in engineering* 2000; **47**:1807–1823.
2. Goldak J, Chakravarti A, M B. A new finite element model for welding heat sources. *Metallurgical Transactions B* 1984; **15**:299–305.
3. Zhang Y, Mabrouki T, Nelias Y D Gong. Chip formation in orthogonal cutting considering interface limiting shear stress and damage evolution based on fracture energy approach. *Finite Elements in Analysis and Design* 2011; **47**(7):850–863.

4. Zhang Y, Mabrouki T, Nelias N, Courbon C, Rech J, D Gong Y. Cutting simulation capabilities based on crystal plasticity theory and discrete cohesive elements. *Journal of Materials Processing Technology* 2012; **212(4)**:936–953.
5. Balagangadhar D, Dorai1 G, Tortorelli D. A displacement-based reference frame formulation for steady-state thermo-elasto-plastic material processes. *International Journal of Solids and Structures* 1999; **36(16)**:2397–2416.
6. Nguyen Q, Rahimian M. Mouvement permanent d'une fissure en milieu elastoplastique. *Journal de Mecanique appliquee* 1981; **5**:95–120.
7. Viriyauthakorn M, Caswell B. Finite element simulation of viscoelastic flow. *Journal of No-Newtonian Fluid Mechanics* 1980; **6**:245–267.
8. Brooks A, Hughes E. Streamline upwind/petrov-galerkin methods for advection dominated flows. *In Proceedings of the Third Conference on Finite Element Methods in Fluid Flows*, Banff, Canada, 1980; 283–292.
9. Ryckelynck D, Gallimard L, Jules S. Estimation of the validity domain of hyper-reduction approximations in generalized standard elastoviscoplasticity. *Advanced Modeling and Simulation in Engineering Sciences* 2015; **2**:1–19.
10. Yvonnet J, He Q. The reduced model multiscale method (r3m) for the non-linear homogenization of hyperelastic media at finite strains. *Journal of Computational Physics* 2007; **223**:341–368.
11. Ryckelynck D. Hyperreduction of mechanical models involing internal variables. *International Journal for numerical methods in engineering* 2009; **77**:75–89.
12. Amsallem D, Farhat C. Interpolation method for adapting reduced-order models and application to aeroelasticity. *AIAA Journal* 2008; **46(7)**:7499–7506.
13. Kerfriden P, Gosselet P, Adhikari S, Bordas S. Bridging proper orthogonal decomposition methods and augmented newtonkrylov algorithms: An adaptive model order reduction for highly nonlinear mechanical problems. *Computer Methods in Applied Mechanics and Engineering* 2011; **200(5-8)**:850–866.
14. Amsallem D, J Zahr M, Farhat C. Nonlinear model order reduction based on local reduced-order bases. *International Journal for Numerical Methods in Engineering* 2014; **92**:891–916.
15. Heyberger C, Boucard P, Nron D. Multiparametric analysis within the proper generalized decomposition framework. *Computational Mechanics* 2012; **49**:277–289.
16. Barrault M, Maday Y, Nguyen N, Patera A. An empirical interpolation method: application to efficient reduced-basis discretization of partial differential equations. *Comptes Rendus Mathematique* 2004; **339**:667–672.
17. Kerfriden P, Goury O, Rabczuk T, Bordas S. A partitioned model order reduction approach to rationalise computational expenses in nonlinear fracture mechanics. *Computer Methods in Applied Mechanics and Engineering* 2013; **256**:169–188.
18. Zhang Y, Combescure A, Gravouil A. Efficient hyper reduced-order model (hrom) for parametric studies of the 3d thermo-elasto-plastic calculation. *Finite Elements in Analysis and Design* 2015; **102-103**:37–51.
19. Ryckelynck D. A priori hyperreduction method: an adaptive approach. *Journal of Computational Physics* 2005; **202**:346–366.
20. Giacoma A, Dureisseix D, Gravouil A, Rochette M. Toward an optimal a priori reduced basis strategy for frictional contact problems with latin solver. *Computer Methods in Applied Mechanics and Engineering* 2015; **283**:1357–1381.
21. Ladeveze P. *Nonlinear computational structural mechanics*. Springer: New York, 1999.
22. Ladeveze P, Passieux JC, Neron D. The latin multiscale computational method and the proper orthogonal decomposition. *Computer Methods in Applied Mechanics and Engineering* 2010; **199**:1287–1296.
23. Ammar A. The proper generalized decomposition: a powerful tool for model reduction. *International Journal of Material Forming* 2009; **3**:89–102.
24. Chinesta F, Ammar A, Cueto E. Proper generalized decomposition of multiscale models. *International Journal for Numerical Methods in Engineering* 2010; **83**:1114–1132.
25. Boucinha L, Ammar A, Gravouil A, Nouy A. Ideal minimal residual-based proper generalized decomposition for non-symmetric multi-field models application to transient elastodynamics in space-time domain. *Computer Methods in Applied Mechanics and Engineering* 2014; **273**:56–76.
26. Giacoma A, Dureisseix D, Gravouil A, Rochette M. A multiscale large time increment/fas algorithm with time-space model reduction for frictional contact problems. *International Journal for Numerical Methods in Engineering* 2014; **97(3)**:207–230.
27. Aguado J, Huerta A, Chinesta F, Cueto E. Real-time monitoring of thermal processes by reduced-order modeling. *International Journal for Numerical Methods in Engineering* 2015; **102**:991–1017.